DOI: 10.13009/EUCASS2019-342

Gas injection effect on heat transfer and boundary layer instability for space vehicles

*Ivan Egorov *, Anton Obraz **, Natalia Palchekovskaya****and Alexander Fedorov[****]
**Central Aerohydrodynamic Institute*
1 Zhukovsky street, Zhukovsky, Moscow region, Russia
ivan.egorov@tsagi.ru
*** Central Aerohydrodynamic Institute*
1 Zhukovsky street, Zhukovsky, Moscow region, Russia
obraz89@gmail.com
**** Moscow Institute of Physics and Technology*
9 Institutsky pereulok, Dolgoprudny, Moscow region, Russia
nathalie.palchekovskaya@gmail.com
***** Moscow Institute of Physics and Technology*
9 Institutsky pereulok, Dolgoprudny, Moscow region, Russia
fedorov@falt.ru

Abstract
In this work effect of wall normal gas injection on the heat transfer and the boundary-layer stability is investigated for the high-speed flow over two models of space vehicles – the hemispherical model and the model of Exomars project. The heat flux distributions on the body surface are obtained using numerical solutions of the Navier-Stokes equations for laminar axisymmetric flow. It was shown that the transition onset, which was experimentally observed in the boundary layer with injection, is associated with relatively small integral amplification of instability. This indicates that in the experiment laminar-turbulent transition is governed by bypass mechanisms.

1. Introduction

Vehicles entering planetary atmospheres can be thermally protected by covering their surfaces with ablative heat shields. The pyrolysis of such materials converts a thin layer of Thermal Protection System (TPS) into ablative products, which are carried away by the flow. This process can significantly reduce heat fluxes inside the vehicle wall. On the other hand, the ablation of TPS influences laminar-turbulent transition processes in the boundary layer flow [1]: the boundary-layer stability is altered by the effective gas injection from the wall [2, 3]; the body shape is changed and transition can be dominated by roughness (see review [4]). The influence of ablation on laminar-turbulent transition has been intensively studied during the 1960s and 1970s. The review of relevant experiments is presented in [5]. Recently, ablative heat shields have regained attention due to Mars exploration missions [6] and reentry vehicles [7].

In [8] the hypersonic flow past a cylinder with a hemispherical nose was treated experimentally. The nose wall was permeable and gas injection normal to the wall surface was used to simulate the ablation effect. The experiment was conductued in the wind tunnel at Mach number M = 7.32 in the range of unit Reynolds number Re_1 = $(0.64 \div 1.33) \times 10^7$ m^{-1}. The calorimeter probes mounted on the nose were used to measure the heat fluxes. The boundary layer state was identified as laminar, transitional or turbulent by comparing the experimental heat-flux distributions with the corresponding analytical and/or computational distributions for laminar and turbulent flows. In the no injection case, the boundary-layer flow was fully laminar. As the injection rate was increased, the transitional region was detected on the nose and moved progressively toward the stagnation point.

In the present work the configuration [8] is studied numerically with emphasis on: 1) the effect of distributed gas injection on the heat-flux distributions in the laminar flow regimes; 2) the effect of gas injection on stability and the transition onset in the transitional flow regimes. In this work model of descent vehicle of ExoMars project is studied at flow regimes with Mach number M = 8 and Reynolds number Re = 1.7×10^6 $м^{-1}$. The laminar flow fields are

DOI: 10.13009/EUCASS2019-342

obtained by solving the Navier-Stokes equations. The corresponding distributions of heat flux are compared with the experimental data [8] and computations [9]. Stability computations are performed using the local-parallel linear stability theory and the e^N method [10, 11]. These computations are verified by comparisons with the results [12], where the geometry and free stream conditions correspond the experiment [8] but the injection non-uniformity is neglected.

2. Numerical simulation

2.1 Laminar flow over hemispherical model

Numerical simulations of axisymmetric laminar flow fields are performed using the in-house code HSFlow [13,14], where the Navier-Stokes equations are discretized using Total Variation Diminishing (TVD) scheme of finite volume with the second-order approximation in space. A steady solution is obtained using the time relaxation method for solving the discretized system on structured multiblock grids. Computations were performed for air which is treated as perfect gas of specific heat ratio $\gamma = 1.4$ and Prandtl number $Pr = 0.72$. Flow parameters: $M_\infty = 7.32$, $Re_1 = (1.191 \div 1.331)\times 10^7$, $T_\infty = 63.84 \div 68$ K. The viscosity coefficient is calculated using the Sutherland law.
In the no injection case, the boundary conditions on the body surface are:

$$u_w = v_w = w_w = 0, \quad T_w = 300, \qquad (dp/dn)_w = 0 \tag{1}$$

In the non-zero injection cases, the boundary conditions are modified in accord with the experiment [8], where the dimensionless mass flow rate of injected gas, $m \equiv (\rho v)_w$, is given as a function of the longitudinal coordinate $s = R^*\theta$ (**Ошибка! Источник ссылки не найден.**).

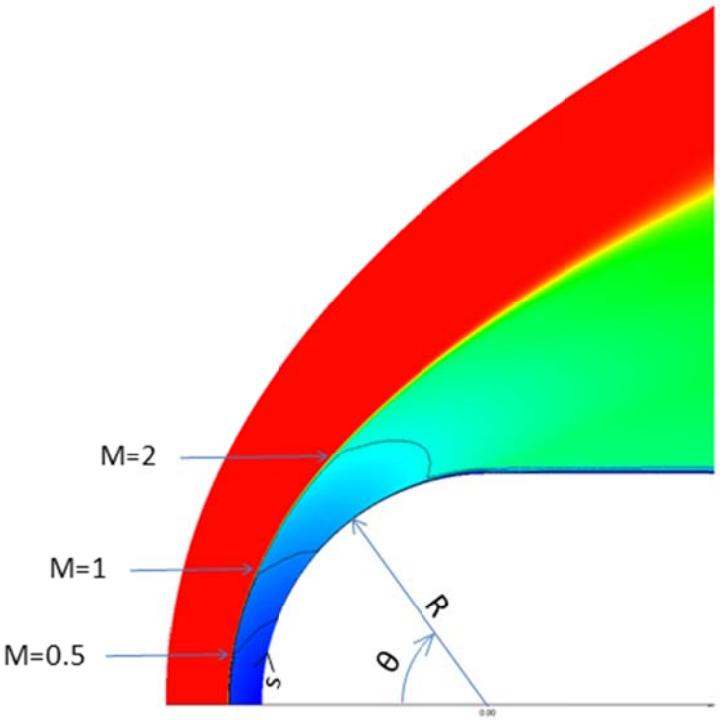

Figure 1: Geometry of the model and the Mach number field

The function $m(s)$ is taken from [8] where the distributions $m(s)$ are provided in table form. These distributions are interpolated using third order polynomials. For each distribution $m(s)$ the corresponding nominal value of the

DOI: 10.13009/EUCASS2019-342

injection rate is determined as $m_* = m(s_*)$, where $s_* = R^*\pi/2$ is the point of juncture between hemispherical nose and cylindrical afterbody. A typical distribution of $m(s)$ is shown in Figure 2 at the nominal value $m_* = 0.003$. Because the external wall pressure decreases with s, the mass flow rate monotonically increases versus θ and attains its maximum at $s = s_*$: $m_* = \max(m(s))$. The injected gas temperature is assumed equal to the wall temperature. The boundary conditions on the body surface are:

$$\rho_w v_w = m(s) \tag{2}$$

$$u_w = w_w = 0;\ T_w^* = 300K \tag{3}$$

The boundary condition for pressure is obtained using the *y*-momentum conservation near the wall [9]:

$$p_w + \rho_w v_w^{\,2} = p_1 + \rho_1 v_1^{\,2} \tag{4}$$

Here the subscript "1" corresponds to the first cell above the body surface. For small values of $\rho_w v_w \sim 0.01$, that is typical for the cases considered, we get $\rho_w v_w^{\,2} = m^2/\rho_w \sim 10^{-4}/\rho_w$. Typical pressure and density on the upper boundary-layer edge at $m(s) = 0$ are: $p_{\theta=0} \approx 0.9$, $p_{\theta=\pi/2} \approx 0.1$, $\rho_{\theta=0} \approx 10.0$ and $\rho_{\theta=\pi/2} \sim 1.0$. Since the ratio $\rho_w v_w^{\,2}/p_w \sim 10^{-5} - 10^{-4}$ is small, the boundary condition $p_w = p_1$ is valid with sufficiently high accuracy. Thus for relatively small values of the nominal injection rate, $m_* < 0.1$, the approximate boundary condition is used:

$$\frac{\partial p}{\partial \mathbf{n}} = 0 \tag{5}$$

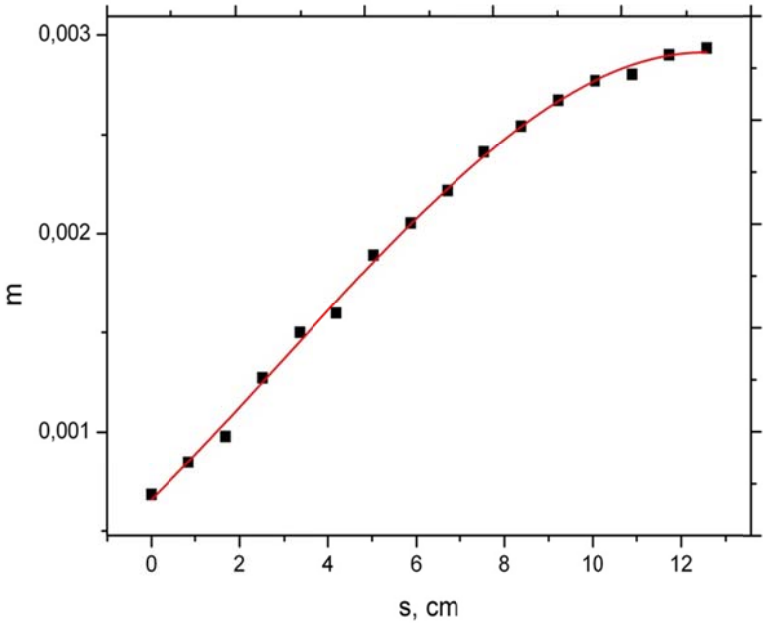

Figure 2: Distribution of the mass flow rate at the nominal value. The black squares – experiment [8], red curve – approximation used in the present work

In Ref. [9] the laminar flow fields are calculated using the code VULCAN and the boundary conditions (2) – (4) with the injection of constant mass flow rate $m(s) = m_*$. To verify our code we performed similar computations using the HSFlow code with the boundary conditions (2), (3) and (5). Figure 3 compares the profiles $u^*(y^*)$ in the stations of $\theta = \pi/16$ and $\pi/4$ at $m(s) = m_* = 0.04$. In our computations, the axisymmetric numerical grid is orthogonal to the body surface in the boundary layer. The grid has 500x500 cells in the longitudinal and normal directions, respectively. There are approximately 120 nodes across the boundary layer in the mid station of $\theta = \pi/4$ and approximately 300 nodes in the longitudinal direction along the spherical part. It is seen that our results agree

DOI: 10.13009/EUCASS2019-342

well with the numerical results [12]. It is also no note here that the e-N calculations of [12] were repeated in the present work and a good agreement was achieved with the discrepancy of N-factors within 5%.

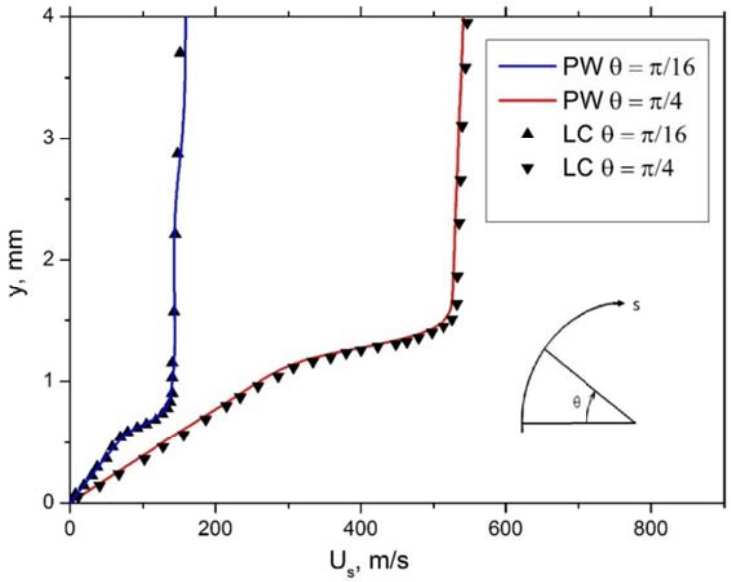

Figure 3: Comparison of the velocity profiles at the injection of constant mass-flow rate . "PW"- present work, "LC" – results of Li et al [12]

Figure 4 shows distributions of the heat flux along the body surface, which is normalized by the heat flux at the stagnation point without injection, for 0., 0.004, 0.01 and 0.013. Here the numerical results are compared with both the experiment [8] and the computations [9]. The distributions, obtained using HSFlow and LAURA [9], agree well in the vicinity of stagnation point (the relative discrepancy does not exceed 10%). The discrepancy can be related to different numerical methods used in HSFlow and LAURA codes. For cases of no injection and small injection rate (0 and 0.004) the numerical results are close to the experimental data. For relatively strong injection (0.01 and 0.013) a significant discrepancy is observed in the vicinity of stagnation point. However, this discrepancy decreases with *s* and the agreement becomes satisfactory in the region of 8 cm. Note that in the experiment [8] the nominal injection rates 0.01 and 0.013 correspond the cases where laminar-turbulent transition is observed on the nose (the transition onset point is 7.5 cm and 6.2 cm, respectively).

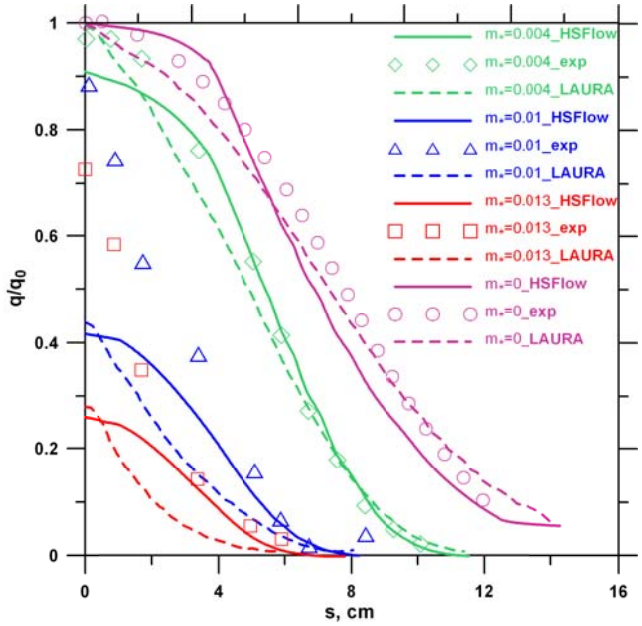

Figure 4: Experimental and numerical distributions of the normalized heat flux at m^* = 0, 0.004, 0.01 and 0.013

DOI: 10.13009/EUCASS2019-342

2.2 Laminar flow over ExoMars vehicle model

On the second stage of investigations flow over descent space vehicle model of ExoMars project with injection normal to the wall surface. Front surface of the model is considered (Figure 5) due to the fact that simulated ablation process takes place mostly on this part of the vehicle. Navier-Stokes equations in axisymmetric statement are chosen for the problem simulation. Perfect gas model is used with effective adiabatic exponent $\gamma = 1.3$.
For calculations the regime is chosen with maximum Reynolds number on the descent trajectory $Re = 1.7 \cdot 10^6$ m^{-1} and Mach number M = 8. For this regime intensities of normal injection are chosen m = 0.01 and m = 0.013, which are constant along the model surface. On the outer boundary of computational domain free stream boundary condition is set with Mach number $M_\infty = 8$ and temperature $T_\infty = 220$ K, on the wall surface injection values $m = \rho V_n = \text{const}$ and radiation conditions are set. In result of numerical simulation flow fields are obtained in the vicinity of front surface of the space vehicle. In Figure 6 fields of Mach number and temperature are shown for regime without gas injection. On the Mach number field sonic line M = 1 is shown.

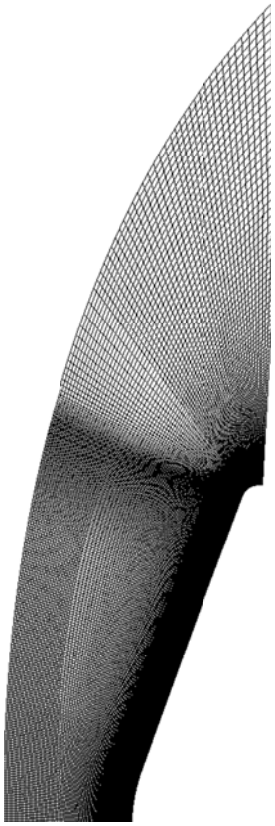

Figure 5: Geometry of front surface of ExoMars space vehicle model and computational grid

DOI: 10.13009/EUCASS2019-342

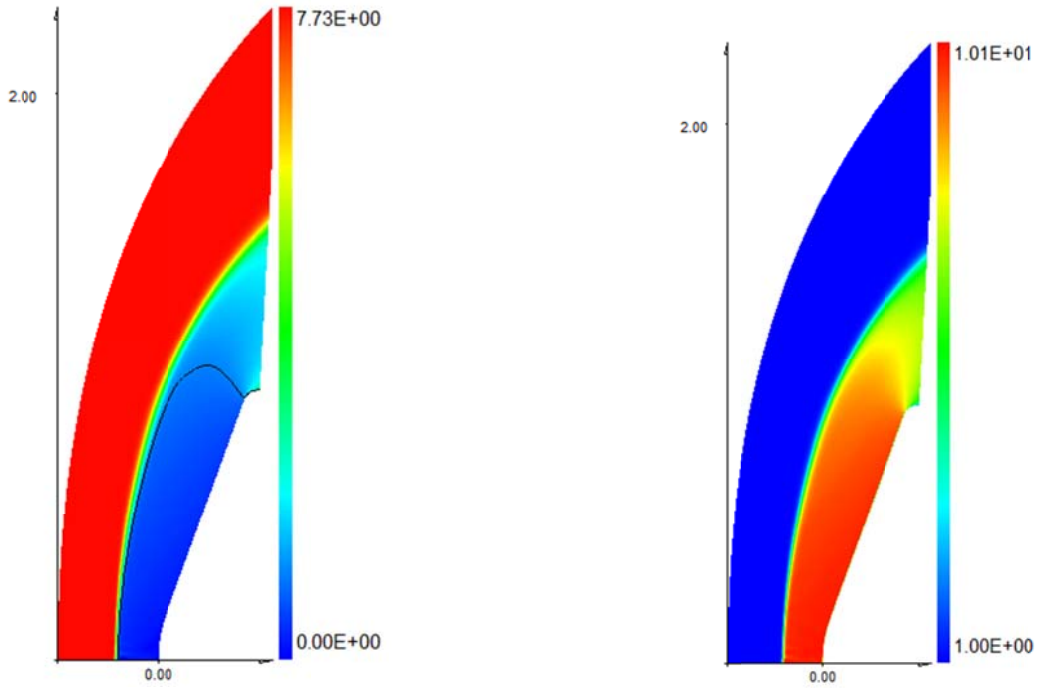

Figure 6: Fields of Mach number (left) and temperature (right) for Exo Mars space vehicle model

In Figure 7 distribution of static pressure along the model surface is given for three regimes: without injection (m=0), and with injection intensities m = 0.01 and m = 0.013. It is seen that in all cases pressure gradient is favorable.

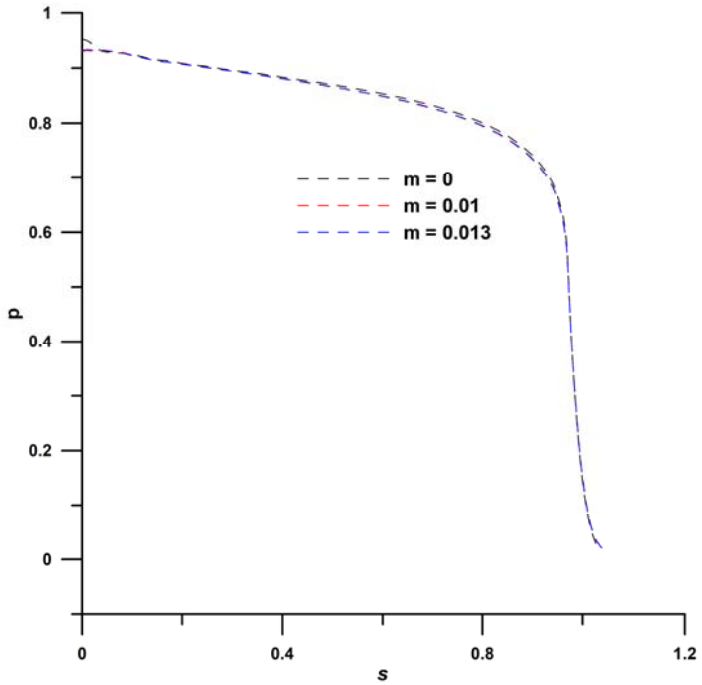

Figure 7: Pressure distribution along the model surface for three flow regimes

DOI: 10.13009/EUCASS2019-342

Influence of injection intensity on heat flux on the model surface is studied. In Figure 8 distributions of normalized heat flux for three regimes are shown: without injection (m = 0) and with injection intensities m = 0.01 and m = 0.013. Heat flux for all regimes is divided by its value at stagnation point for regime without gas injection. It should be noted that value of normalized heat flux at stagnation point is nearly ten times greater without gas injection of given intensities. This result also qualitatively agrees with results of [8]. It should be noted that for this model of space vehicle heat flux is more sensitive to gas injection, than for hemispherical model.

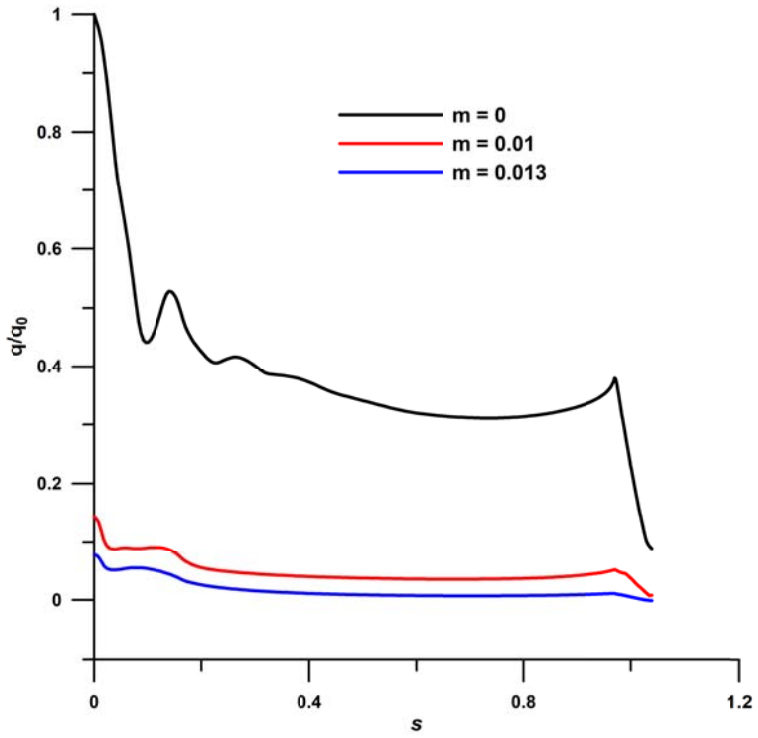

Figure 8: Distributions of normalized heat flux for three flow regimes

2.3 Stability computations

Linear stability computations were performed using the stability module [15] of the HSFlow code. The spatial local-parallel stability problem is solved for disturbances of the convective wave form

$$\mathbf{q}'(s,y^*,z^*,t^*) = \hat{\mathbf{q}}(y^*)\exp\left(i \int\limits_{s_0(\beta,\omega)}^{s} \alpha^*(\beta,\omega,s)ds + i\beta^* z^* - i\omega^* t^* \right) \qquad (6)$$

Here $\mathbf{q}' = (u',v',w',p',T')^T$ and $\alpha^* = \alpha_r^* + i\alpha_i^*$ is a complex eigenvalue depending on angular frequency ω^* and transverse wave number β^*, $s_0(\beta^*,\omega^*)$ is the upstream neutral point.

On the spherical nose considered, the local Mach numbers at the upper boundary-layer edge correspond to subsonic or low supersonic flow. The boundary layer thickness y_s for stability computations (boundary layer edge) is found using the tangential velocity derivative: $y_s = Cy_{0.1}$, where $C = 7.0$ is a constant value, and $y_{0.1}$ is the first position moving from outside the boundary layer where the derivative becomes larger than 10% of its maximum value inside the boundary layer. The sonic line is located at $s_s \approx 6.4$ cm ($\theta_s \approx 40^\circ$) and it weakly depends on the injection rates considered. In the no injection case, all modes of the discrete spectrum decay; i.e. the boundary layer flow is stable on the nose. This is due to the favorable pressure gradient, which has a well-known stabilizing effect on the waves of Tollmien-Schlichting (TS) type. These findings agree with the experimental observations [8] and the stability computations [12].

DOI: 10.13009/EUCASS2019-342

At a certain nominal mass flow rate $m_{*,cr}$ the boundary layer becomes unstable. The point $s = s_{cr}$, where instability is observed for the first time, is called hereafter as a critical stability point (in some papers this point is called as a neutral stability point). At $m_* = 0.007$ the boundary layer is still stable on the spherical nose, while at $m_* = 0.01$ the critical stability point is located near the sonic point: $s_{cr} \approx 6.5$ cm. Here the most unstable are plane waves of $\beta = 0$, and their eigenfunctions resemble those of TS-waves on a flat plate under similar flow conditions at the upper boundary-layer edge. Calculations show that upstream of the sonic point the most amplified are plane waves. Therefore, further stability computations were performed for plane waves of $\beta = 0$. Their downstream growth was modelled using the e^N method. For various frequencies ω, the integral amplification is computed as

$$n(s,\omega) = -\int_{s_0(\omega)}^{s} \alpha_i^*(0,\omega,s)ds \qquad (7)$$

As shown in Figure 9, the envelopes of amplification curves $N(s) = \max_{\omega^*} n(s,\omega^*)$ strongly depend on the nominal injection rate m_*. The critical point s_{cr}, where $N(s_{cr}) = 0$, rapidly moves upstream from $s_{cr} \approx 6.5$ cm to $s_{cr} = 1.4$ cm as m_* increases from 0.01 to 0.021.

At the experimentally determined transition onset points the N-factors are small: $N(s_{tr}) < 1.5$ for the all injection rates considered (see the dashed lines in Figure 9). This indicates that the linear amplification stage of laminar-turbulent transition is bypassed in the wind-tunnel experiment [8]. Nevertheless, Figure 10 shows that the critical points, predicted by the linear stability theory, correlate well with the empirical points of the transition onset. Thus, the nonlinear breakdown seems to be correlated with the linear instability mechanism. The assumption of whether this correlation has a physical basis can be checked by direct numerical simulations and/or detailed measurements of the controlled disturbances on the model tested in a quiet hypersonic wind tunnel.

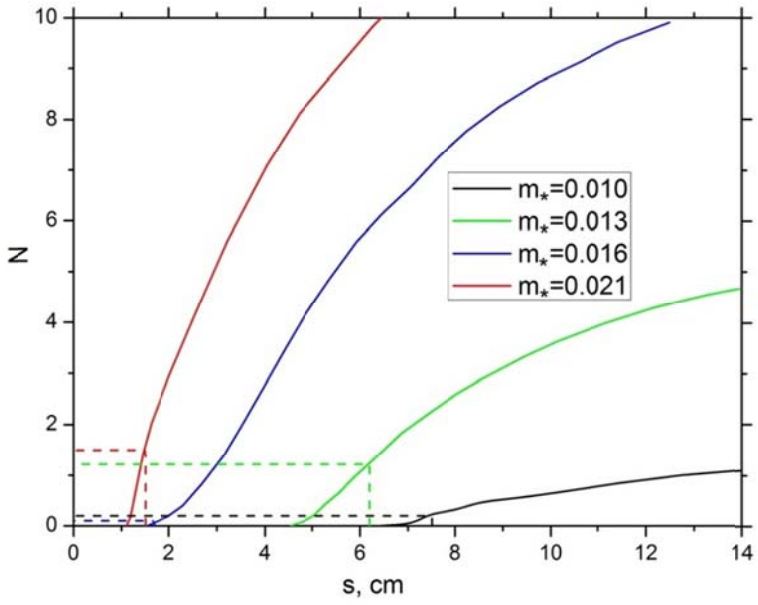

Figure 9: The envelopes $N(s^*)$ at various nominal injection rates m_*. The dashed lines correspond to N at the experimentally observed transition onsets points

DOI: 10.13009/EUCASS2019-342

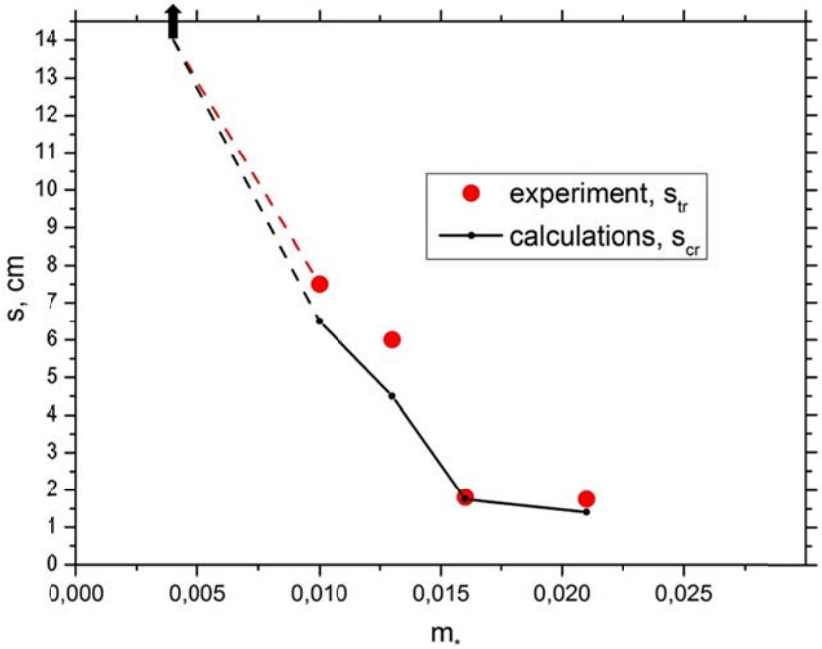

Figure 10: The correlation between the computed critical points $s_{cr}(m_*)$ (black line) and the transition onset points $s_{tr}(m_*)$ (red circles) measured in [8]. The black arrow indicates that the flow is laminar and stable all over the nose surface.

3. Conclusions

The effect of normal gas injection on heat transfer and stability of the boundary layer flow was investigated with the help of CFD solutions for the laminar (undisturbed) flow and the local-parallel linear stability theory. Nonuniform distributions of the injection mass flow rates were specified accurately using the experimental data. It was shown that the transition onset, which was experimentally observed in the boundary layer with injection, is associated with relatively small integral amplification of instability, $N(s_{tr}) < 1.5$. This indicates that in the experiment laminar-turbulent transition is governed by bypass mechanisms. Nevertheless, the empirical transition onset points correlate well with the critical stability points predicted by the linear stability theory. This correlation might be useful for engineering estimations of the ablation rate at which laminar-turbulent transition is likely to occur on the nose of high-speed vehicle.

This work was performed at the Moscow Institute of Physics and Technology and supported by the Russian Foundation for Basic Research (project no. 17-08-00969) (calculations) and Russian Science Foundation (project no. 19-19-00470) (numerical technique development).

References

[1] Morkovin, M.V. 1969. Critical evaluation of transition from laminar to turbulent shear layers with emphasis on hypersonically traveling bodies. Air Force Flight Dynamics Laboratory. Technical Report AFFDL-TR-68-149, DTIC citation AD-686178.

[2] Scott, C. J., and Anderson, G. E. 1958. Boundary-layer transition with gas injection. *Journal of the Aerospace Sciences*. 25: 791.

DOI: 10.13009/EUCASS2019-342

[3] Pappas, C. C., and Okuno, 1964. A. heat-transfer measurement for binary gas laminar boundary layers with high rates of injection. Ames Research Center. Technical Note TN-D-2473, NASA, Washington, D.C..

[4] Reda, D. C. 2002. Review and synthesis of roughness-dominated transition correlations for reentry applications. *Journal of Spacecraft and Rockets.* 39:161–167.

[5] Schneider, S. 2010. Hypersonic boundary-layer transition with ablation and blowing. *Journal of Spacecraft and Rockets*. 47:225–237.

[6] Merrifield, J. A., Gulhan, A., Neeb, D. 2014. Rough wall heat flux augmentation analysis in the framework of the ExoMars project. AIAA Paper 2014–2817.

[7] Johnston, C. O., Gnoffo P.A., Mazaheri, A. 2012. Study of ablation–flowfield coupling relevant to the Orion heat shield. *Journal of Thermophysics and Heat Transfer*. 26:213–221.

[8] Kaattari, G. E. 1978. Effects of mass addition on blunt body boundary layer transition and heat transfer. NASA, TP-1139.

[9] Gnoffo, P. A., and Thompson R.A. 2008. Implementation of a blowing boundary condition in the LAURA code. AIAA Paper 2008–1243.

[10] Smith, A. M. O., and Gamberoni, N. 1956. Transition, pressure gradient and stability theory. Douglas Aircraft Company, ES 26388.

[11] Van Ingen, J. L. 1956. A suggested semi-empirical method for the calculation of the boundary layer region. TU Delft. Technical Report VTH-74.

[12] Li, F., Choudhari M., Chang C.L., White, J. 2013. Effects of injection on the instability of boundary layers over hypersonic configurations. *Physics of Fluids.* 25:1–16.

[13] Palchekovskaya, N. V., Novikov, A.V., and Egorov, I.V. 2018. Numerical simulation of the flow over a segment-conical body on the basis of Reynolds equations. *Computational Mathematics and Mathematical Physics*. 58:118–129.

[14] Novikov, A., Egorov, I., and Fedorov, A. 2016. Direct numerical simulation of wave packets in hypersonic compression-corner flow. *AIAA Journal*. 54: 2034–2050.

[15] Fedorov, A. V., and Obraz, A.O. 2017. The high-speed flow stability (HSFS) software package for stability analysis of compressible boundary layers. *TsAGI Science Journal*. 48:223–242.